Adsorption of furan, hexanoic acid, and alkanes in a hierarchical zeolite at reaction conditions: Insights from molecular simulations

Tyler R. Josephson [a,*], Paul J. Dauenhauer [b], Michael Tsapatsis [b,c], J. Ilja Siepmann [a,b]

[a] *Department of Chemistry and Chemical Theory Center, University of Minnesota, Minneapolis, MN 55455, United States*
[b] *Department of Chemical Engineering and Materials Science, University of Minnesota, Minneapolis, MN 55455, United States*
[c] *Department of Chemical and Biomolecular Engineering, John Hopkins University, Baltimore, MD 21218, United States*

ARTICLE INFO

ABSTRACT

Hierarchical zeolites containing both micropores and mesopores are valuable catalysts for facilitating reactions of large molecules. Furan acylation by fatty acids is a promising reaction for valorizing biomass, and the self-pillared pentasil (SPP) zeolite was found to perform particularly well for this reaction. To better understand the distribution of molecules in hierarchical zeolites at the elevated temperature ($T = 523$ K) and the elevated pressure ($p > 1$ bar) associated with typical reaction conditions, unary and binary adsorption were predicted using Monte Carlo simulations in the isothermal–isobaric Gibbs ensemble. Adsorption of six species (furan, hexanoic acid, *n*-hexane, *n*-decane, *n*-tetradecane, and 3,6-diethyloctane) was investigated from vapor, liquid, and supercritical phases, and loadings into the micropores, onto the mesopore surface, and in the mesopore interior of SPP were obtained. As pressure increases, *n*-alkanes fill the micropores before loading the surface and then the interior of the mesopore, while furan and hexanoic acid adsorb strongly to the mesopore surface due to hydrogen bonding interactions with surface silanols. Hydrogen bonding interactions also draw hexanoic acid molecules in the micropore region toward the pore mouths, so their carboxylic acid group forms H-bonds with silanols, while the alkyl tails interact with the micropore walls. Mesopore condensation is observed for molecules below their critical point, and occurs when the Gibbs free energy of transfer into the mesopore interior and onto the mesopore surface converge. When hexanoic acid adsorption occurs in the presence of alkane solvents, then the selectivity and spatial distribution of hexanoic acid in the micropores and on the surface can be tuned by adjusting the fluid pressure and the alkane length and/or branching.

1. Introduction

Hierarchical materials integrate micropores with larger mesopores to enable high-performance catalysis [1,2]. Micropores control catalysis through molecule-scale confinement [3,4] and mesopores provide additional surface area and allow bulky molecules to access catalytic sites [5]. Mesoporous zeolites can enhance diffusion relative to conventional zeolites under some conditions, though transport phenomena in hierarchical materials is complex [6]. These qualities make them useful catalysts for a wide range of chemistries. As complex multiscale materials, they also exhibit rich thermodynamic and transport behavior in adsorption [7–11] and catalysis [12–14].

One useful catalyst is the self-pillared pentasil (SPP) class of zeolite, a hierarchical zeolite with a "stack-of-cards" geometry arising from intergrown 2D nanosheets of MFI zeolite [15,16]. With 2–8 nm mesopores formed between nanosheets and 0.6 nm micropores in the MFI framework, SPP has enabled high yields in numerous catalytic processes including methanol-to-olefins [17], glucose isomerization to fructose [5] and butadiene synthesis from tetrahydrofuran [18]. While several studies have examined fundamentals of adsorption, transport [6,19], and catalysis [14,20] in SPP, it can be difficult to characterize these phenomena under reaction conditions.

In this work, we investigate the adsorption processes involved in the synthesis of oleo-furan sulfonate (OFS) surfactants via furan acylation with fatty acids [21]. These bio-based surfactants use a furan-based polar head group (from sugar dehydration) with a fatty acid-derived hydrocarbon tail (from plant and algae oils). While they have similar critical micelle concentrations to petroleum-derived linear alkyl benzene sulfonates, OFS exhibit superior hard-water stability [21]. Furthermore, chain length, branching, and functionalization can be customized to tailor surfactants to specific applications [21].

* Correspondence to: Department of Chemical, Biochemical, and Environmental Engineering, University of Maryland, Baltimore County, Baltimore, MD 21250, United States.
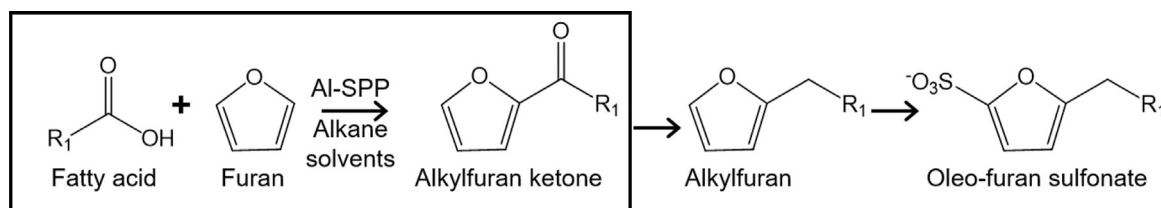*E-mail address:* tjo@umbc.edu (T.R. Josephson).

Fig. 1. Synthesis of oleo-furan sulfonate surfactants. The adsorption of fatty acid, furan, and alkanes occurring during the Al-SPP catalyzed acylation reaction are the subject of this work.

OFS are synthesized in a multi-step process: (1) acylation of furan with fatty acid, (2) hydrogenative dehydration of the product alkylfuran ketone, and (3) sulfonation to form OFS (Fig. 1). The bottleneck in this process is the acylation step [21]; selective hydrogenation and sulfonation are established commercial processes. The highest-performing catalyst was found to be Al-SPP with 89% yield to alkylfuran ketone [21].

Prior studies of acylation on zeolites have pointed to the importance of understanding and regulating competitive adsorption [22–24]. Specifically, these explore acylation in a related system: toluene and anisole by acetic anhydride on Brønsted acidic zeolites. Through the use of adsorption measurements, batch reactions, and kinetic modeling, these studies demonstrate how catalytic reaction performance is influenced by competitive adsorption, in particular, the deactivation of the catalyst due to adsorption of the reaction product. Recent work by Ji, et al. on furan acylation by fatty acids on H-MFI specifically probed furan acylation under flow conditions, by reacting acetic acid and hexanoic acid with furan and 2-methylfuran [25]. Steady state operation was achieved with nearly 100% selectivity at 523 K, but only when acid is in excess; when furan or 2-methylfuran is in excess, they polymerize and produce coke, even at room temperature. The authors measured adsorption of acetic acid, furan, and 2-methylfuran using temperature-programmed desorption, finding both furans and acetic acid adsorb strongly to Brønsted acid sites. Due to low polymerization rates in excess acid, the authors infer that in competitive adsorption conditions, acid either outcompetes furan in binding to the Brønsted acid site, or at least prevents a second furan from reaching the first one adsorbed to the acid site [25]. However, little is known about how these molecules adsorb under reaction conditions, especially on the hierarchical SPP material; the objective of the present work is to probe the adsorption and phase behavior of furan, fatty acids, and hydrocarbons at reaction conditions in the absence of Brønsted acid sites.

We use configurational-bias Monte Carlo simulations [26] in the isothermal–isobaric version of the Gibbs ensemble [27] to probe adsorption in all-Si SPP of reactants and alkane solvents in furan acylation at $T = 523$ K. We compare adsorption from vapor, liquid, and supercritical phases of hexanoic acid, furan, n-hexane, n-decane, n-tetradecane, and 3,6-diethyloctane, where the latter is selected as a sorbate that does not adsorb in MFI due to steric limitations. We investigate the spatial distribution of the sorbate molecules in the micropores, mesopore surface, and mesopore interior of SPP. We also consider mixtures of hexanoic acid and alkanes to investigate the role that solvent selection plays in the distribution of adsorbates throughout the material.

2. Methods

Simulations were performed in the isobaric–isothermal version of the Gibbs ensemble [27–29] using the Monte Carlo for Complex Chemical Systems-Minnesota (MCCCS-MN) software [30]. Trial moves included translations, rotations, and dual-cutoff [31] coupled-decoupled configurational-bias Monte Carlo (CD-CBMC) moves [26,32,33] to sample configurations within each simulation box, as well as inter-box swap moves [34,35] to equilibrate chemical potentials between the simulation boxes. Volume moves were performed only on the box

representing the fluid reservoir [36]. Analysis of regional adsorption was performed using a modified version of the MCFlow software [37].

Alkane solvents were modeled using the transferable potentials for phase equilibria-united atom (TraPPE-UA) force field for linear [38] and branched [26] alkanes. Hexanoic acid was modeled by combining alkane parameters from TraPPE-UA with parameters from the acetic acid force field by Kamath et al. [39]. Furan was modeled as a rigid nine-site model using the explicit-hydrogen TraPPE-EH model [40]. The SPP zeolite was treated as semi-flexible, with rigid Si and O atoms and flexible hydrogens on the silanols. The bulk of the SPP zeolite was modeled using TraPPE-zeo [41], while the Lennard-Jones and partial charge parameters for the silanol groups were adopted from previous work [42,43]. A cutoff distance of 14 Å was used for the adsorbate–adsorbate and adsorbate–zeolite interactions in the zeolite phase, with analytical tail corrections applied for Lennard-Jones interactions and Ewald summation for the Coulomb interactions beyond this cutoff [41, 44]. A larger cutoff at approximately 40% of the box length was used for low-density vapor phases. The SPP structure was generated starting with a $3 \times 3 \times 3$ supercell of MFI (using the ORTHO structure of MFI, with coordinates from van Koningsveld et al. [45]) from which a $2 \times 2 \times 3$ section was removed and dangling oxygen atoms were converted to silanols [11] (see Fig. 2). This process produces a mesopore with a volume fraction of 44% (of the total volume) bound by MFI nanosheets with a thickness of 20 Å. The dimensions of the zeolite box were 60.066 $\times$ 59.697 $\times$ 40.149 Å.

Each adsorption simulation was initialized with an empty zeolite box (i.e., reflects the adsorption branch for cases with adsorption hysteresis); to avoid nucleation issues in the reservoir box, this box was initialized as a low-density gas when $p < p_{\mathrm{vap}}$ or as a high-density liquid when $p > p_{\mathrm{vap}}$. Four independent simulations were performed, each with at least 50,000 MC cycles of equilibration and 60,000 MC cycles of production. To analyze the adsorption behavior, three domains of SPP are distinguished in Fig. 2: micropore (micro), mesopore surface (surf), and mesopore interior (meso). The "mesopore surface" of SPP begins at the O atoms of the silanol groups, extending into the mesopore domain for 6 Å. With this definition, 55.66% of the SPP volume is microporous, 22.7% is the mesopore surface, and 21.7% is mesopore interior. The number density in each region is measured by locating each sorbate molecule's center of mass and sorting it into one of these three regions, totaling the population in each region, and normalizing by the volume of the region. The free energy of transfer from the fluid phase to any of these regions can be computed from the ratio of number densities [46,47]

$$\Delta G_{\mathrm{fluid} \to \mathrm{zeo}} = -RT \ln\left(\frac{\rho_{\mathrm{zeo}}}{\rho_{\mathrm{fluid}}}\right) \tag{1}$$

where ρ_{zeo} is the number density in a specific region of the zeolite box. Eq. (1) can also be used to compute free energies of transfer between regions, e.g. from the mesopore to the micropore.

Hydrogen bonding with surface SiOH of SPP was analyzed for furan (H-bond acceptor), and hexanoic acid (both donor and acceptor). The criteria for an H-bond required $d_{\mathrm{O-HO}} < 2.5$ Å and $\theta_{\mathrm{OHO}} > 90°$ [48,49]. Molecules were labeled as H-bonded to the surface if they participated in at least one H-bond with an SiOH, whether as donor or acceptor; H-bonded adsorbates were further classified based on their center of mass as adsorbed into the micropore or the surface region as defined in Fig. 2 (none were located in the mesopore).
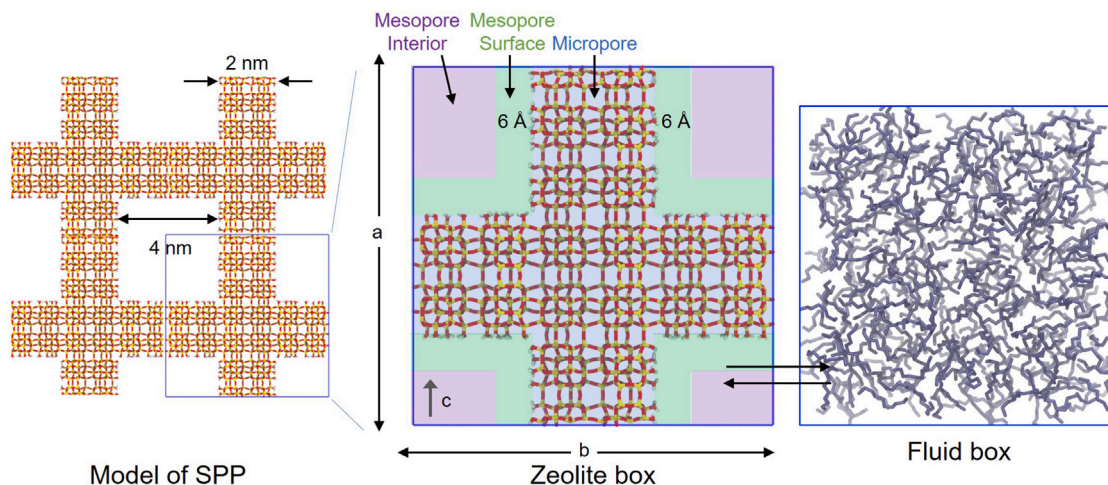
Fig. 2. Model of the SPP zeolite with adsorption regions shaded in different colors. The fluid box shows liquid *n*-decane at $p = 64$ bar and $T = 523$ K.

Table 1

Vapor pressures for hexanoic acid, *n*-decane, *n*-tetradecane, and 3,6-diethyloctane at $T = 523$ K. The uncertainties of the simulation data are reported as the standard error of the mean from 16 independent simulations. Experimental values for *n*-decane are from NIST [50] and for *n*-tetradecane from Morgan and Kobayashi [51].

Compound	Simulation p_{vap} [bar]	Experiment p_{vap} [bar]
Hexanoic acid	5.56_7	
n-decane	5.93_6	5.028
n-tetradecane	1.194_{11}	0.931
3,6-diethyloctane	3.25_6	

3. Results and discussion

3.1. Vapor pressure

For compounds with a critical temperature above 523 K, the vapor pressures were obtained using simulations in the NVT-Gibbs ensemble (see Table 1). For *n*-decane and *n*-tetradecane, the TraPPE-UA model over predicts p_{vap} by 18 and 28%, respectively. Experimental data are not available for hexanoic acid and 3,6-diethyloctane; the prediction for the former falls slightly below that for *n*-decane and that for the latter is about midway between the two linear alkanes, as would be expected from the number of carbon atoms.

3.2. Unary adsorption

Single-component adsorption was investigated at $T = 523$ K, for furan from $p = 1$ bar to $p = 64$ bar and for all other species from $p = 1/64$ bar to $p = 64$ bar. The upper bound of this range is higher than the critical pressures of *n*-hexane and furan (30.2 and 53.2 bar, respectively [50]). The unary adsorption isotherms in SPP are compared in Fig. 3. At low pressures, the less volatile species adsorb most strongly, with loading in the following order: *n*-tetradecane > hexanoic acid > *n*-decane > *n*-hexane > furan. However, 3,6-diethyloctane is an outlier showing a loading similar to *n*-hexane despite its much lower volatility. For sorbate molecules with $T_c > 523$ K, the loading shows a jump before reaching saturation. *n*-tetradecane saturates SPP around $p = 1/2$ bar, 3,6-diethyloctane saturates SPP around $p = 2$ bar, and hexanoic acid and *n*-decane saturate SPP around $p = 4$ bar. These pressures are approximately $0.6p_{vap}$. In contrast, $p = 64$ bar is not sufficiently high to achieve saturation loading for *n*-hexane and furan at $T = 523$ K. At the highest pressure, efficient packing generally drives differences in loading, with smaller molecules packing more efficiently; furan > hexanoic acid > *n*-hexane > *n*-decane > *n*-tetradecane > 3,6-diethyloctane. At even higher pressure, the loading for *n*-hexane will
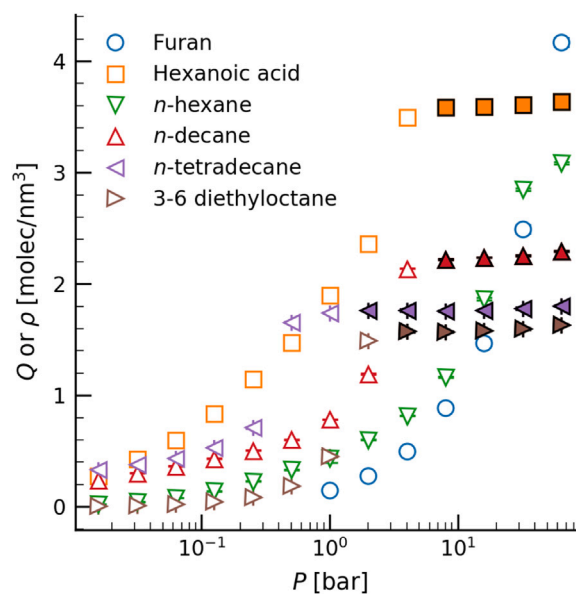

Fig. 3. Predicted unary adsorption loadings for furan, hexanoic acid, and alkanes. Filled symbols indicate adsorption from a liquid phase.

exceed that of hexanoic acid. The lower loading for 3,6-diethyloctane than for *n*-tetradecane already indicates that the micropore region is not accessible for this branched molecule.

3.2.1. Reactants: Furan and hexanoic acid

At pressures below 20 bar, furan exhibits the lowest adsorption loading of the compounds investigated here (see Fig. 3). At all pressures, furan preferentially adsorbs onto the mesopore surface as indicated by the higher number density in this region (see Fig. 4). At low pressures, adsorption in the mesopore interior is enhanced by only a factor of 1.2 due to weak interactions with the nanosheets in comparison to the density of furan in the superheated vapor phase. However, at higher pressures ($p > 32$ bar), adsorption density in the mesopore interior exceeds that in the micropores, even approaching the density in the mesopore surface region near 64 bar. This is commensurate with an increase in the density of the fluid phase; because furan is above its critical temperature (490 K [40]), there is no phase change in the fluid as its density increases. In contrast, adsorption density in the micropores is initially enhanced by a factor of 7 but, actually, becomes
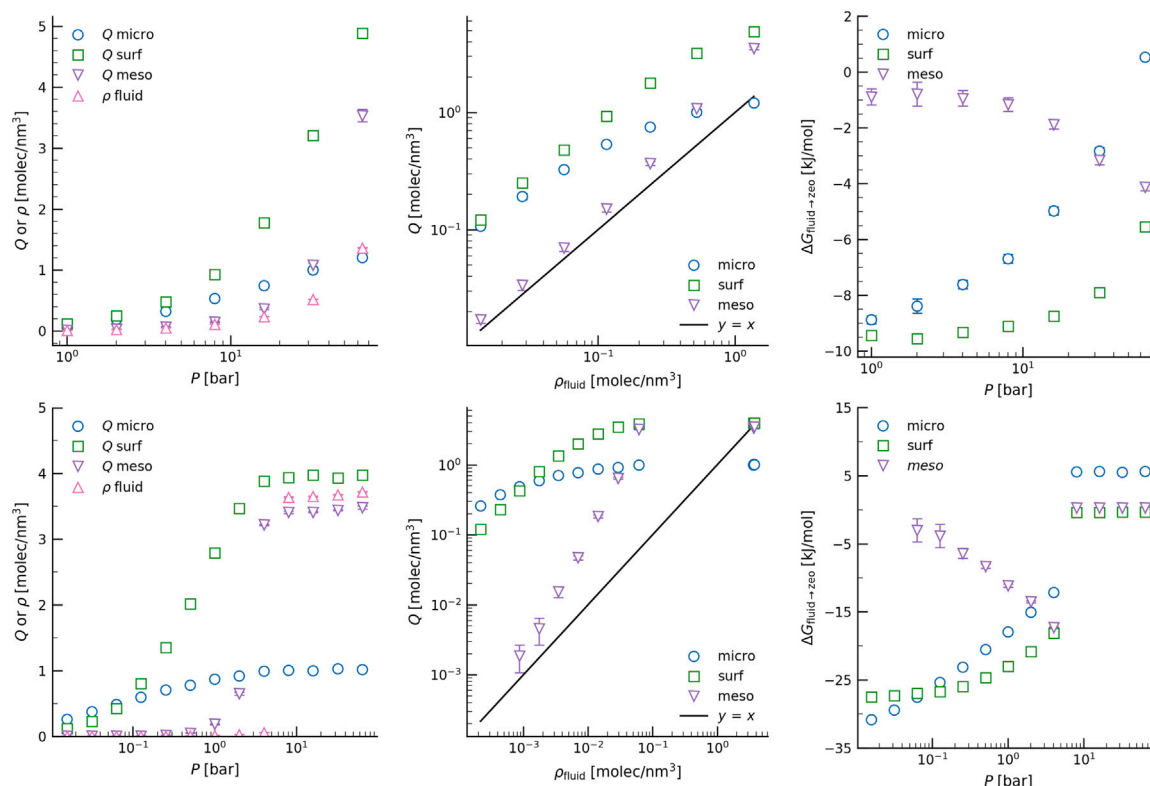
Fig. 4. Loading as function of pressure (left) and density (middle) and Gibbs free energy of adsorption (right) into the different SPP regions for furan (top) and hexanoic acid (bottom).

unfavorable at the highest reservoir density due to the entropic cost of loading in the highly confined environment.

ΔG_{tr} for furan into the mesopore surface and micropore regions of SPP are about −9.5 and −8.8 kJ/mol, respectively, at $p = 1$ bar, and become increasingly less favorable as pressure increases due to an increase in entropic cost as these regions start to fill (see Fig. 4). This increase is more pronounced for the micropore region. ΔG_{tr} into the mesopore interior is much less favorable at −1 kJ/mol at 1 bar, but becomes more favorable at increasing pressures due to stronger sorbate–sorbate interactions, surpassing that of the micropore above 32 bar.

H-bonding with the silanols helps to drive furan adsorption (a snapshot is shown in Fig. 5); 36_4% of surface-adsorbed furan are participating in H-bonds at $p = 1$ bar (see Fig. 5). As loading increases, more molecules adsorb to the surface and the fraction of H-bonded furans on the surface decreases to 24.1_3% at $p = 64$ bar. 82% to 89% of the H-bonded furans have their center of mass in the surface region; the remainder is positioned at pore mouths of the MFI channels, with centers of mass in the micropore region. These constitute only a small fraction (3.4_5% to 4.76_{14}%) of furans in the micropores.

At $p = 1/64$ bar, hexanoic acid adsorbs into the micropores with a highly negative ΔG_{tr} of $−30.8_2$ kJ/mol (see Fig. 4). As pressure increases, hexanoic acid loading on the mesopore surface increases, and at 1/8 bar, the density in the surface region exceeds that in the micropore. Loading on the mesopore surface increases steadily until approaching saturation near 4 bar. The loading in the mesopore interior is negligible (and statistically insignificant for $p \leq 1/32$ bar) until it begins to increase around 1 bar. The isotherm in the mesopore interior is much steeper than that in the micropore and the surface, with a step change in density between 2 and 4 bar, akin to a phase change, before it fully saturates by 8 bar.

As pressure increases, $\Delta G_{fluid \rightarrow micro}$ and $\Delta G_{fluid \rightarrow surf}$ are significantly more favorable than $\Delta G_{fluid \rightarrow meso}$. They begin to converge with increasing pressure, and when $\Delta G_{fluid \rightarrow meso} \approx \Delta G_{fluid \rightarrow surf} \approx −18$ kJ/mol, condensation in the mesopore occurs, after which the entire zeolite

is saturated. These changes occur while hexanoic acid is in the vapor phase; the fluid phase does not condense until 5.56_7 bar (see Table 1). For adsorption from the liquid phase, $\Delta G_{fluid \rightarrow surf} \approx \Delta G_{fluid \rightarrow meso} \approx 0$ kJ/mol, whereas $\Delta G_{fluid \rightarrow micro}$ is unfavorable at 5 kJ/mol.

Mesopore condensation occurs due to a shift of the vapor–liquid coexistence curve within the confines of the mesopore, as previously observed for simulations of Lennard-Jonesium in a slit pore [52] and experimentally for gases in a controlled-pore glass [53]. This also conforms to a Type IV isotherm, according to IUPAC classification [54]. The IUPAC classification was primarily established to facilitate characterization of micro- and mesoporous materials via small molecules adsorbing under cryogenic conditions (e.g. N_2 and Ar). Here, we observe analogous behavior for hexanoic acid at a much higher temperature (while $T < T_c$), as previously noted by Severson and Snurr for n-alkanes in carbon slit pores [55]. Interactions with the pore walls and with molecules adsorbed at the pore wall that lead to mesopore condensation are also present for furan, but here $\Delta G_{fluid \rightarrow meso}$ decreases only to −4 kJ/mol.

H-bonding is much stronger for hexanoic acid than for furan (see Fig. 5) because the former possesses two H-bond acceptor sites and can also act as H-bond donor. At $p = 1/64$ bar, 95.5_8% of the acid molecules in the surface region participate in H-bonds with SiOH. As pressure increases, the ratio of surface-adsorbed acid molecules in H-bonds decreases gradually to 80.7_6% for $p \geq 4$ bar, when mesopore condensation occurs. The molecules on the mesopore surface form strong H-bonds at low pressure, but when loading increases, not all acid molecules in the surface region are able to form H-bonds to SiOH. The reduction in fraction of surface H-bonds between $p = 1/4$ and $p = 4$ bar coincides with a decreased magnitude in $\Delta G_{fluid \rightarrow surf}$.

Because hexanoic acid's hydrophobic tail interacts favorably with the micropore walls through dispersion interactions, a substantial fraction of the H-bonded molecules have their center of mass in the micropore region; 45_2% of H-bonded molecules protrude into the micropores at $p = 1/64$ bar, but this decreases to 24_2% when adsorbing
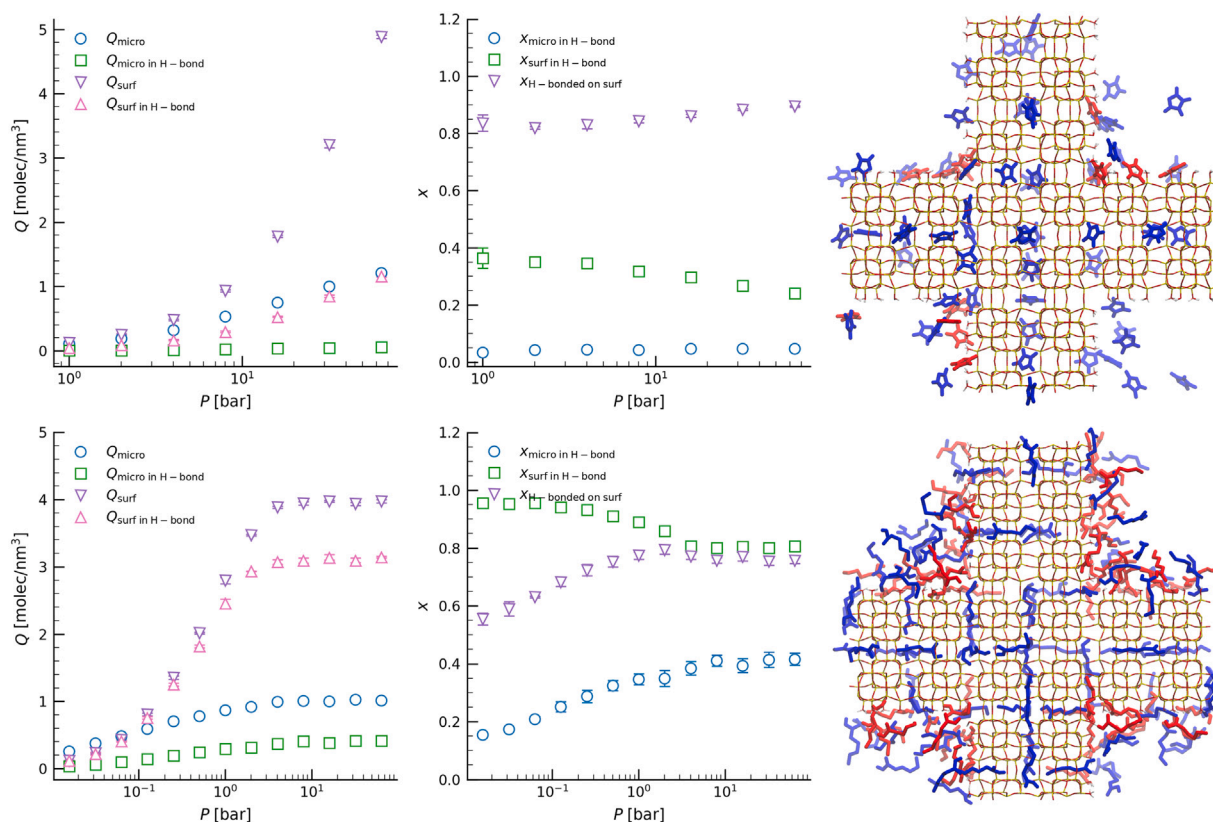
Fig. 5. H-bonding of furan (top) and hexanoic acid (bottom) to SiOH groups in SPP, and snapshots at $p = 8$ bar and $p = 1$ bar, respectively. $x_{\text{micro in H-bond}} = N_{\text{micro}}^{\text{H-bonding with SiOH}} / N_{\text{micro}}^{\text{total}}$ is the fraction of molecules in the micropores forming H-bonds with SiOH. $x_{\text{surf in H-bond}} = N_{\text{surf}}^{\text{H-bonding with SiOH}} / N_{\text{surf}}^{\text{total}}$ is the fraction of molecules in the surface region participating in H-bonds with SiOH. $x_{\text{H-bonded on surf}} = N_{\text{surf}}^{\text{H-bonding with SiOH}} / N_{\text{surf+micro}}^{\text{H-bonding with SiOH}}$ is the fraction of H-bonded adsorbate molecules located in the surface region (the remaining are in the micropores). In the snapshots, red adsorbates are H-bonded to surface SiOH, while blue adsorbates are not. (For interpretation of the references to color in this figure legend, the reader is referred to the web version of this article.)

from the liquid phase. As the loading in the micropores increases, the fraction of micropore-adsorbed acid forming H-bonds with the surface increases from 15_1% at $p = 1/64$ bar, to 42_2% when the zeolite is saturated. This illustrates a complex interplay between dispersion interactions between the micropore walls and the alkane tails, and H-bonding between surface SiOH and the acid head group. At low p, hexanoic acid is distributed throughout the micropores; when loading is low, dispersion interactions are favored. As pressure increases, additional molecules are preferentially added to the mesopore surface and the regions of the micropores that allow H-bonding with SiOH. At saturation and when adsorbing from the liquid phase, the most favorable distribution in the micropores is achieved by locating acid head groups near the surface to H-bond with SiOH, with the alkane tails in the micropores or laying across the pore mouths. We speculate that these configurations may be favorable for catalysis, anchoring the alkane tails in the micropore while providing access on the surface for reactions with adsorbed furan.

3.2.2. Solvents: Linear and branched alkanes

Adsorption of three linear and one branched alkane solvent was also studied to examine the influence of alkane chain length and branching on adsorption behavior. At 523 K, n-hexane is supercritical, whereas n-decane, n-tetradecane, and 3,6-diethyloctane are subcritical, with vapor pressures falling in the range from 1 to 6 bar (see Table 1). Here 3,6-diethyloctane was selected because its architecture (spacing between branch points and length of the side chains) effectively prevents adsorption in the micropores of MFI.

As previously found by Bai et al. [11] for linear alkanes with 6 to 9 carbon atoms, the three n-alkanes studied here preferentially adsorb into the micropores at low pressures (see Fig. 6); longer n-alkanes

adsorb more strongly, $q_{\text{C14}}^{\text{micro}} > q_{\text{C10}}^{\text{micro}} > q_{\text{C6}}^{\text{micro}}$. At high pressures, the micropores become saturated, and packing enables higher loadings of shorter chains, with $q_{\text{C6}}^{\text{micro}} > q_{\text{C10}}^{\text{micro}} > q_{\text{C14}}^{\text{micro}}$. A Henry's law region with constant $\Delta G_{\text{fluid}\to\text{micro}}$ is only observed here for n-hexane, whereas lower reservoir pressures would be needed for the longer n-alkanes to access the Henry's law region. Beyond the Henry's region, $\Delta G_{\text{fluid}\to\text{micro}}$ increases nearly linearly with increasing $\log p$, then jumps to about +5 kJ/mol for adsorption from liquid or highly compressed supercritical fluid phases. $\Delta G_{\text{fluid}\to\text{micro}}$ values at low pressure are more favorable for longer n-alkanes, but the larger entropic cost due to reduced conformational freedom leads to a larger increase with increasing pressure for the longer n-alkanes. At $p = 1$ bar, fortuitously, the $\Delta G_{\text{fluid}\to\text{micro}}$ values for all three n-alkanes are close to -16 kJ/mol.

As observed for furan and hexanoic acid, surface loading for each n-alkane increases in the intermediate pressure range (see Fig. 6). Longer n-alkanes exhibit onset of adsorption on the surface at lower pressures than shorter n-alkanes, and also exhibit steeper adsorption profiles. At high pressures, the surface becomes saturated; longer n-alkanes saturate the surface sooner due to stronger interactions of the larger number of methylene units with the zeolite nanosheets, while shorter alkanes exhibit a higher saturation loading due to more efficient packing of smaller molecules. In contrast to hexanoic acid, the surface densities for n-decane and n-tetradecane reach only about 50% of saturation loading before mesopore condensation occurs. Given the lengths of these n-alkanes, a fraction of the molecules adsorbs only partially with one terminus onto the mesopore surface while their center of mass is found in the mesopore interior. Even at supercritical conditions for n-hexane, the steepest increases in the mesopore surface and interior loadings are shifted to pressures lower by factors of 4 and 2, respectively, than for the reservoir phase.
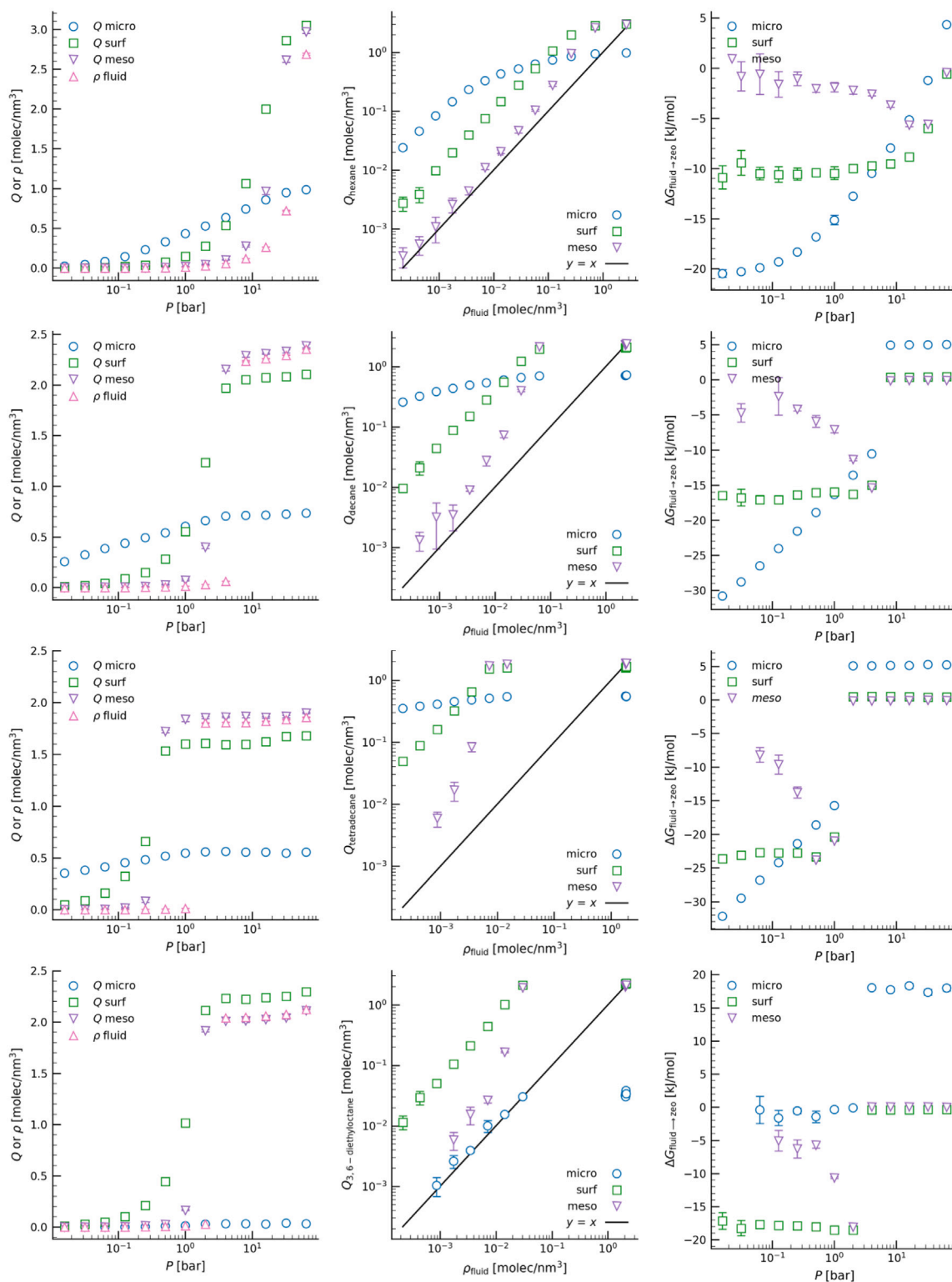
Fig. 6. Loading as function of pressure (left) and density (middle) and Gibbs free energy of adsorption (right) into the different SPP regions for (a) *n*-hexane, (b) *n*-decane, (c) *n*-tetradecane, and (d) 3,6-diethyloctane.

Without the ability for H-bonding interactions with the surface silanols, *n*-alkanes do not adsorb as strongly to the surface as hexanoic acid. From $p = 1/8$ to 4 bar, the Gibbs free energy of adsorption of hexanoic acid varies from −26 to −18 kJ/mol; i.e., the decrease in available silanol groups leads to a significant increase with increasing pressure. In contrast, $\Delta G_{\text{fluid}\rightarrow\text{surf}}$ remains fairly constant for adsorption of *n*-decane and *n*-tetradecane from the gas phase and also for

n-hexane at fluid densities below 0.2 molec/nm³. For the *n*-alkanes, the $\Delta G_{\text{fluid}\rightarrow\text{surf}}$ values for adsorption from low-density fluid phases are regularly spaced with −10, −17, and −24 kJ/mol for *n*-hexane, *n*-decane, and *n*-tetradecane, respectively. Each methylene unit added to the alkane chain increases $\Delta G_{\text{fluid}\rightarrow\text{surf}}$ by approximately 7/4 kJ/mol. For adsorption from the liquid phase (or a highly compressed supercritical phase), $\Delta G_{\text{fluid}\rightarrow\text{surf}}$ values are close to zero.

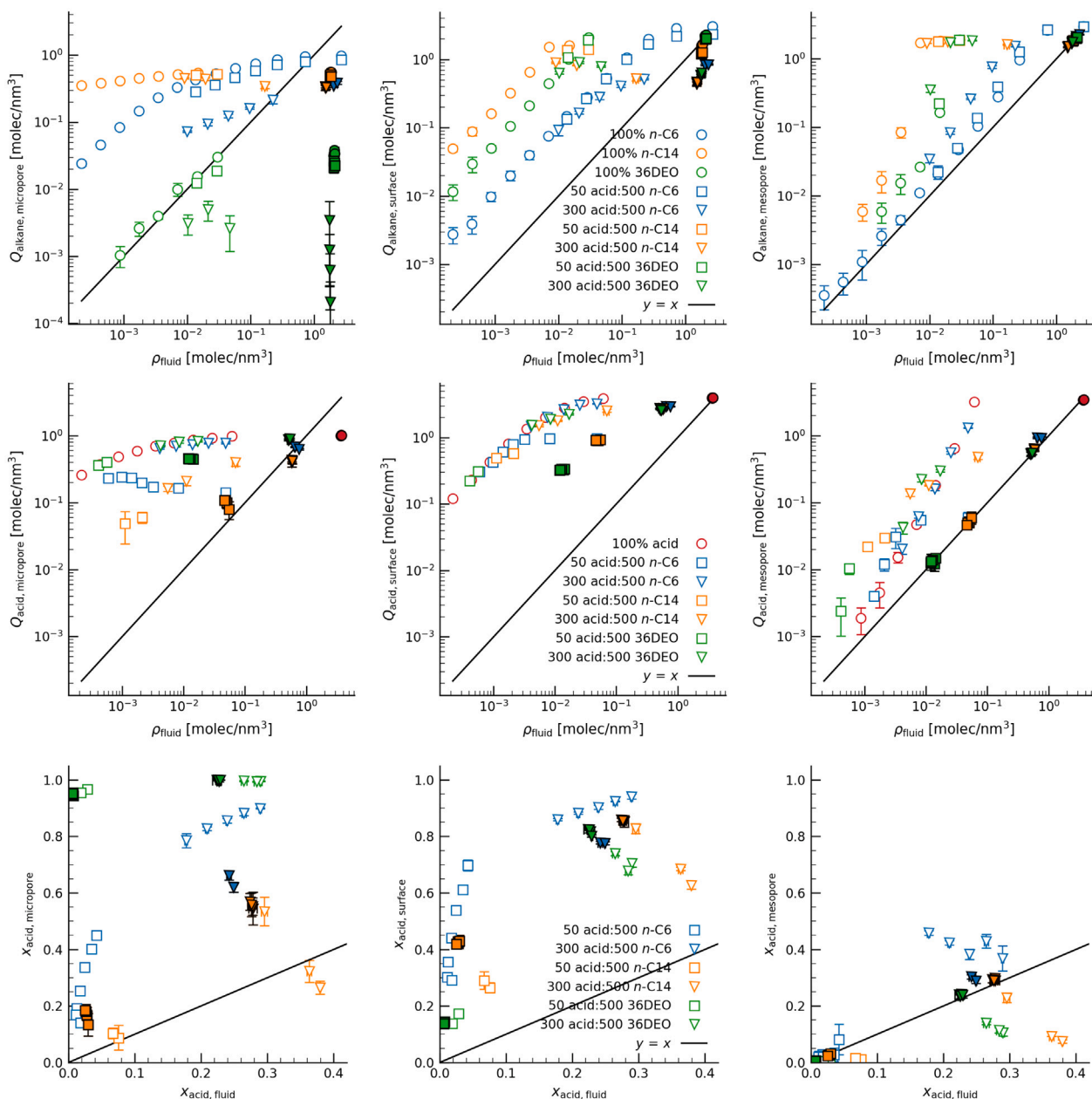**Fig. 7.** Adsorption into the micropore (left), mesopore surface (middle), and mesopore interior (right) regions of SPP from binary mixtures of hexanoic acid and *n*-hexane (*n*-C6), *n*-tetradecane (*n*-C14), and 3,6-diethyloctane (36DEO). Simulations were initialized with mixture compositions of 50 or 300 hexanoic acid molecules and 500 alkane molecules. Filled symbols indicate adsorption from a liquid phase.

As with the micropores and the mesopore surface, the mesopore interior is loaded first with the longer alkanes, but at the highest pressures, the short alkanes pack more efficiently. Mesopore condensation is clearly observed for *n*-tetradecane and *n*-decane, with step-change adsorption in the mesopore occurring at $p = 1/2$ bar and $p = 4$ bar, respectively. Again, we observe $\Delta G_{\text{fluid}\rightarrow\text{meso}} \approx \Delta G_{\text{fluid}\rightarrow\text{surf}}$ at mesopore condensation.

Hexanoic acid and *n*-decane provide an interesting comparison, because these compounds have comparable vapor pressures (see Table 1), yet different chemical functionality. At 2 bar, just before mesopore condensation, $\rho_{\text{acid}}^{\text{surf}}$ reaches 87% of the maximum value of $\rho_{\text{acid}}^{\text{surf}}$ observed; the surface is essentially saturated before mesopore condensation occurs. In contrast, $\rho_{\text{C10}}^{\text{surf}}$ reaches 58% of the maximum value of $\rho_{\text{C10}}^{\text{surf}}$ observed. This enhanced acid loading on the surface does not significantly change the pressure at which mesopore condensation occurs; both species exhibit mesopore condensation between 2 and 4 bar.

When the reservoir phase is in vapor or supercritical states, the density in the mesopore is always higher than the density in the reservoir, on account of the weak interactions that molecules in the mesopore feel from the pore walls and other molecules adsorbed on the surface. Even at 64 bar, when *n*-decane and *n*-tetradecane are liquids, the density in the mesopore is slightly higher than the fluid density ($\rho_{\text{fluid}} = 2.354_2$ molec/nm^2 and $\rho_{\text{mesopore}} = 2.39_2$ molec/nm^2 for *n*-decane, and $\rho_{\text{fluid}} = 1.858_3$ and $\rho_{\text{mesopore}} = 1.899_5$ for *n*-tetradecane). In contrast, the surface density of the alkanes is lower than the liquid density. However, caution is needed because these observations focus on the location of a molecule's center of mass (that is needed for calculation of the Gibbs free energy). For longer alkanes, not all of the segments will fall into the same region as the center of mass. Prior simulation studies have shown enhanced segmental densities near planar surfaces [56,57]. However, this behavior is distinct from hexanoic acid at saturation, where the trend is reversed. The saturation density in the mesopore is slightly lower (3.48_2 molec/nm^3) than the fluid density (3.723_6 molec/nm^3),
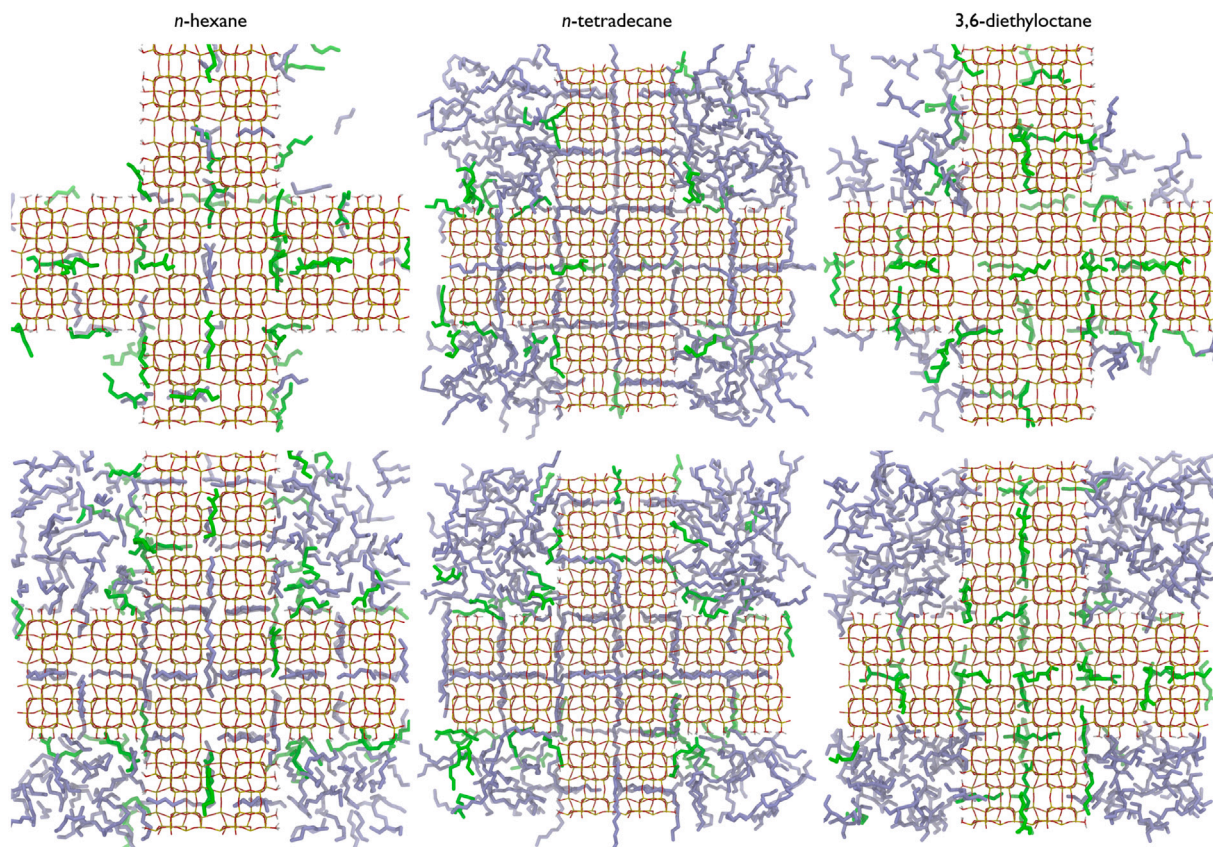
Fig. 8. Snapshots illustrating the loading of hexanoic acid (green) and alkane solvent (purple) molecules into SPP. Loadings are shown for binary mixtures of hexanoic acid and *n*-hexane (left), *n*-tetradecane (middle), and 3,6-diethyloctane (right) at $p = 1$ bar (top) and $p = 64$ bar (bottom). The simulations include 50 hexanoic acid molecules and 500 alkane molecules distributing between reservoir (not shown) and SPP. The reservoir is in a vapor state at $p = 1$ bar and in a dense liquid-like state at $p = 64$ bar.

while the surface density is slightly greater (3.97_3 molec/nm³). For hexanoic acid, H-bonding interactions result in a tighter packing on the surface with many of the non-polar tails pointing into the mesopore interior but the center of mass still always being in the surface region.

By design, the adsorption behavior of 3,6-diethyloctane differs markedly from the linear alkanes. As seen in Fig. 6d, loading in the micropores is disfavored compared to those in the mesopore surface and interior regions. For adsorption from the gas phase, the loading density in the micropores is similar to the reservoir density (i.e., $\Delta G_{\text{fluid}\rightarrow\text{micro}} \approx 0$ kJ/mol), whereas it is about two orders of magnitude smaller for adsorption from the liquid phase. Adsorption at the mesopore surface is strongly favored, but its $\Delta G_{\text{fluid}\rightarrow\text{surf}} \approx -18$ kJ/mol is comparable to *n*-decane that has two fewer carbon atoms, i.e., the branching also reduces the propensity for surface adsorption. In general, 3,6-diethyloctane's loading behavior on the surface and in the mesopore is comparable to that of *n*-decane and *n*-tetradecane. Mesopore condensation occurs between $p = 1$ and 2 bar, and is preceded by an increase in loading on the surface. Again, $\Delta G_{\text{fluid}\rightarrow\text{meso}} \approx \Delta G_{\text{fluid}\rightarrow\text{surf}} \approx -18$ kJ/mol at this point.

3.3. Binary adsorption

To investigate competitive adsorption in SPP, we considered binary mixtures of hexanoic acid and alkanes. In particular, how does co-adsorption with solvent affect the loading of hexanoic acid on the surface and in micropores, and how does solvent branching influence the distribution of molecules in the micro/mesoporous environment? Simulations with 500 solvent molecules (either *n*-hexane, *n*-tetradecane, or 3,6-diethyloctane) and 50 or 300 hexanoic acid molecules were performed at $T = 523$ K and p ranging from 1 to 64 bar. Adsorption loadings for each species in each region of SPP are reported in Fig. 7, and representative snapshots of the system are shown in Fig. 8.

3.3.1. Micropores

In the micropores of SPP, adsorption of hexanoic acid can be significantly altered through co-adsorption of solvent molecules. Presence of 3,6-diethyloctane generally does not significantly affect adsorption of hexanoic acid in the micropores because this solvent is largely excluded from this region. In this case, these mixtures show hexanoic acid loadings comparable to that from pure hexanoic acid at the same hexanoic acid number density in the fluid phase. The exception to this rule is the 50:500 acid:3,6-diethyloctane mixture at higher pressures where the reservoir phase condenses and lowers the chemical potential of hexanoic acid compared to a unary vapor phase at the same hexanoic acid number density ($\rho_{\text{fluid}} \approx 10^{-2}$ molec/nm³). The presence of hexanoic acid in the mixture further lowers the already very low loading of 3,6-diethyloctane. Together these lead to extremely high selectivity for hexanoic acid in the micropore; the mole fraction of hexanoic acid in the micropores is > 95%, even when the mole fraction in the fluid is < 2% (see Figs. 7 and 8).

At low pressure, hexanoic acid loading in the micropores decreases by an order of magnitude in the presence of *n*-tetradecane, whereas the solvent loading is less affected (see Fig. 7). These conditions exhibit little selectivity for either sorbate in the micropores. As pressure increases, the micropore loading of hexanoic acid increases more rapidly than for *n*-tetradecane because hexanoic acid is smaller and packs more efficiently. For the hexanoic acid/*n*-hexane mixtures, the 50:500 and 300:500 mixtures have significantly different behavior (see Fig. 7). For the former mixture, the loading of hexanoic acid in the micropores is significantly lower and, actually, decreases with increasing number density in the fluid phase (which corresponds to an increase in pressure), as replacing hexanoic acid with the smaller *n*-hexane, which is entropically favorable. In contrast, *n*-hexane loading is only slightly lowered. As pressure increases, the mole fraction of hexanoic acid in

the micropore decreases from 45% to less than 15%. The effects are less pronounced for the 300:500 mixture. Here the *n*-hexane loading is decreased by a factor of about 4, whereas the hexanoic acid loading is only slightly decreased. This leads to acid mole fractions of about 80% in the micropores.

Comparing the three solvents, we find that a highly branched solvent can induce near 100% adsorption selectivity in the micropores, a light solvent such as *n*-hexane also leads to substantial enrichment, with $x_{\mathrm{acid,zeo}}$ significantly above the parity line, whereas a heavy *n*-alkane can displace hexanoic acid from the micropores.

3.3.2. Mesopore surface

Hexanoic acid is always enriched on the mesopore surface relative to the fluid phase. For light and heavy *n*-alkane solvents, $x_{\mathrm{acid,zeo}}$ on the mesopore surface is greater than $x_{\mathrm{acid,zeo}}$ in the micropores (see Fig. 7). This is due to the favorable H-bonding interactions with surface silanols — interactions that favor hexanoic acid over all alkanes. For 3,6-diethyloctane, however, the micropore enrichment is even larger due to steric hindrance for micropore adsorption. On the surface, loadings of hexanoic acid from mixtures are comparable to unary adsorption at lower pressures, though at higher pressures, competition from solvent causes reduced loading on the surface. For example, in the 50:500 acid: *n*-hexane system, at the lowest number densities (low pressures), surface loading is low and competition is not significant, however, as pressure increases, hexanoic acid loading is reduced in comparison to the unary loading as the *n*-alkanes displaces it on the surface (see Figs. 7 and 8). Concurrently, the *n*-alkane loading on the mesopore surface is lowered in the presence of hexanoic acid. Similar as for the micropore loading, an alkane-rich liquid solution constitutes a more hospitable environment than the vapor phase for hexanoic acid; thus, at the same hexanoic acid number density, the loading is lowered by about a factor of 8 for liquid- versus vapor-phase adsorption. Nevertheless, the mole fraction enrichment is larger for liquid-phase adsorption because of the higher entropic penalty for adsorption of *n*-tetradecane and 3,6-diethyloctane.

3.3.3. Mesopore interior

The mesopore interior always shows a higher number density than the fluid phase when adsorbing from vapor, due to weak dispersion interactions with the mesopore walls and adsorbates in the surface region (see Fig. 7). Generally, co-adsorption causes hexanoic acid and solvent loadings to exceed unary adsorption at the same number density because the unlike interactions also contribute to favorable interactions in the mesopore interior. For vapor-phase adsorption, hexanoic acid shows compositional enrichment in the mesopore interior for the mixture with the more volatile *n*-hexane solvent, whereas hexanoic acid exhibits depletion when co-adsorbing with the less volatile *n*-tetradecane and 3,6-diethyloctane solvents. For adsorption from the liquid phase, the compositions in the reservoir and the mesopore interior are essentially the same.

4. Conclusions

Adsorption of furan, hexanoic acid, and alkane solvents were investigated into Si-SPP under reaction conditions. Species below their critical point exhibited mesopore condensation following an enrichment of mesopore surface-adsorbed species. As mesopore condensation is approached, $\Delta G_{\mathrm{fluid \to meso}}$ becomes more favorable and reaches $\Delta G_{\mathrm{fluid \to surf}}$, and a value near -18 kJ/mol is found here for hexanoic acid, *n*-decane, *n*-tetradecane, and 3,6-diethyloctane.

H-bonding interactions with hexanoic acid drive saturation of the surface prior to mesopore condensation. Absence of H-bonding in *n*-decane, which has a comparable vapor pressure to hexanoic acid, leads to less surface enrichment, but does not significantly shift the pressure at which mesopore condensation occurs. H-bonding of hexanoic acid to the surface contributes to its stronger free energies of adsorption compared to the alkanes, but these interactions become less important as the surface saturates with acid and the number of H-bonds per acid molecule decreases. Up to a third of the hexanoic acid molecules adsorbed in the micropore region also form H-bonds on the surface; the dispersion interactions draw the alkyl tails to the zeolite micropore walls, while H-bonding draws the carboxylic acid head groups to the pore mouths and corners of the mesopore framework. In binary mixtures of hexanoic acid and alkanes, the solvent chain length and degree of branching can be used to control the distribution of hexanoic acid in the various regions of the zeolite. Hexanoic acid selectively adsorbs to the mesopore surface due to favorable H-bonding interactions with silanols. Hexanoic acid is also mostly enriched in the micropores, though can be displaced by *n*-hexane at high pressures or by *n*-tetradecane at low pressures. In mixtures with a highly branched solvent, hexanoic acid adsorbs with nearly 100% selectivity in the micropores due to the molecular sieving nature of the zeolite.

CRediT authorship contribution statement

Tyler R. Josephson: Conceptualization, Data curation, Formal analysis, Investigation, Methodology, Project administration, Software, Validation, Visualization, Writing - original draft, Writing - review & editing. **Paul J. Dauenhauer:** Conceptualization, Funding acquisition, Project administration, Writing - review & editing. **Michael Tsapatsis:** Conceptualization, Funding acquisition, Writing - review & editing. **J. Ilja Siepmann:** Conceptualization, Methodology, Software, Validation, Visualization, Funding acquisition, Supervision, Writing - review & editing.

Declaration of competing interest

The authors declare that they have no known competing financial interests or personal relationships that could have appeared to influence the work reported in this paper.

Acknowledgments

Appendix. Supporting information

CSV files containing the data in the figures, source codes for the version of MCCCS-MN [30] and MCFlow [37] used for this manuscript, as well as sample input files containing the semiflexible SPP zeolite (fort.4, fort.77, and topmon.inp) and output files (run.production and fort12.production) for one independent simulation are available at https://github.com/SiepmannGroup/SPP_Adsorption.

References

[1] E. Holm, Martin Spangsberg Taarning, K. Egeblad, C.H. Christensen, Catalysis with hierarchical zeolites, Catal. Today 168 (1) (2011) 3–16.

[2] K. Li, J. Valla, J. Garcia-Martinez, Realizing the commercial potential of hierarchical zeolites: New opportunities in catalytic cracking, ChemCatChem 6 (1) (2014) 46–66, http://dx.doi.org/10.1002/cctc.201300345.

[3] R. Gounder, M.E. Davis, Titanium-Beta zeolites catalyze the stereospecific isomerization of d-glucose to l-sorbose via intramolecular C5-C1 hydride shift, ACS Catal. 3 (7) (2013) 1469–1476, http://dx.doi.org/10.1021/cs400273c.

[4] A.J. Jones, S.I. Zones, E. Iglesia, Implications of transition state confinement within small voids for acid catalysis, J. Phys. Chem. C 118 (2014) 17787–17800, http://dx.doi.org/10.1021/jp5050095.

[5] L. Ren, Q. Guo, P. Kumar, M. Orazov, D. Xu, S.M. Alhassan, K.A. Mkhoyan, M.E. Davis, M. Tsapatsis, Self-pillared, single-unit-cell Sn-MFI zeolite nanosheets and their use for glucose and lactose isomerization, Angew. Chem. Int. Edn 54 (37) (2015) 10848–10851, http://dx.doi.org/10.1002/anie.201505334.

[6] P. Bai, E. Haldoupis, P.J. Dauenhauer, M. Tsapatsis, J.I. Siepmann, Understanding diffusion in hierarchical zeolites with house-of-cards nanosheets, ACS Nano 10 (8) (2016) 7612–7618, http://dx.doi.org/10.1021/acsnano.6b02856.

[7] H. Wang, L. Huang, Z. Wang, A. Mitra, Y. Yan, Hierarchical zeolite structures with designed shape by gel-casting of colloidal nanocrystal suspensions, Chem. Commun. (15) (2001) 1364–1365, http://dx.doi.org/10.1039/b104275k.

[8] J.C. Groen, L.A. Peffer, J. Pérez-Ramírez, Pore size determination in modified micro- and mesoporous materials. Pitfalls and limitations in gas adsorption data analysis, Microporous Mesoporous Mater. 60 (1–3) (2003) 1–17, http://dx.doi.org/10.1016/S1387-1811(03)00339-1.

[9] M. Thommes, B. Smarsly, M. Groenewolt, P.I. Ravikovitch, A.V. Neimark, Adsorption hysteresis of nitrogen and argon in pore networks and characterization of novel micro- and mesoporous silicas, Langmuir 22 (2) (2006) 756–764, http://dx.doi.org/10.1021/la051686h.

[10] P.A. Monson, Understanding adsorption/desorption hysteresis for fluids in mesoporous materials using simple molecular models and classical density functional theory, Microporous Mesoporous Mater. 160 (2012) 47–66, http://dx.doi.org/10.1016/j.micromeso.2012.04.043.

[11] P. Bai, D.H. Olson, M. Tsapatsis, J.I. Siepmann, Understanding the unusual adsorption behavior in hierarchical zeolite nanosheets, ChemPhysChem 15 (11) (2014) 2225–2229, http://dx.doi.org/10.1002/cphc.201402189.

[12] D. Liu, A. Bhan, M. Tsapatsis, S. Al Hashimi, Catalytic behavior of Brønsted acid sites in MWW and MFI zeolites with dual meso- and microporosity, ACS Catal. 1 (1) (2011) 7–17, http://dx.doi.org/10.1021/cs100042r.

[13] J. García-Martínez, M. Johnson, J. Valla, K. Li, J.Y. Ying, Mesostructured zeolite Y – High hydrothermal stability and superior FCC catalytic performance, Catal. Sci. Technol. 2 (5) (2012) 987–994, http://dx.doi.org/10.1039/c2cy00309k.

[14] D. Xu, O. Abdelrahman, S.H. Ahn, Y. Guefrachi, A. Kuznetsov, L. Ren, S. Hwang, M. Khaleel, S. Al Hassan, D. Liu, S.B. Hong, P. Dauenhauer, M. Tsapatsis, A quantitative study of the structure-activity relationship in hierarchical zeolites using liquid-phase reactions, AIChE J. 65 (3) (2019) 1067–1075, http://dx.doi.org/10.1002/aic.16503.

[15] X. Zhang, D. Liu, D. Xu, S. Asahina, K.A. Cychosz, K.V. Agrawal, Y. Al Wahedi, A. Bhan, S. Al Hashimi, O. Terasaki, M. Thommes, M. Tsapatsis, Synthesis of self-pillared zeolite nanosheets by repetitive branching, Science 336 (6089) (2012) 1684–1687, http://dx.doi.org/10.1126/science.1221111.

[16] D. Xu, G.R. Swindlehurst, H. Wu, D.H. Olson, X. Zhang, M. Tsapatsis, On the synthesis and adsorption properties of single-unit-cell hierarchical zeolites made by rotational intergrowths, Adv. Funct. Mater. 24 (2) (2014) 201–208, http://dx.doi.org/10.1002/adfm.201301975.

[17] R. Khare, A. Bhan, Mechanistic studies of methanol-to-hydrocarbons conversion on diffusion-free MFI samples, J. Catal. 329 (2015) 218–228, http://dx.doi.org/10.1016/j.jcat.2015.05.012.

[18] O.A. Abdelrahman, K.P. Vinter, L. Ren, D. Xu, R.J. Gorte, M. Tsapatsis, P.J. Dauenhauer, Simple quantification of zeolite acid site density by reactive gas chromatography, Catal. Sci. Technol. 7 (17) (2017) 3831–3841, http://dx.doi.org/10.1039/c7cy01068k.

[19] C.C. Chang, A.R. Teixeira, C. Li, P.J. Dauenhauer, W. Fan, Enhanced molecular transport in hierarchical silicalite-1, Langmuir 29 (45) (2013) 13943–13950, http://dx.doi.org/10.1021/la403706r.

[20] T.R. Josephson, R.F. DeJaco, S. Pahari, L. Ren, Q. Guo, M. Tsapatsis, J.I. Siepmann, D.G. Vlachos, S. Caratzoulas, Cooperative catalysis by surface lewis acid/silanol for selective fructose etherification on Sn-SPP zeolite, ACS Catal. (2018) 9056–9065, http://dx.doi.org/10.1021/acscatal.8b01615.

[21] D.S. Park, K.E. Joseph, M. Koehle, C. Krumm, L. Ren, J.N. Damen, M.H. Shete, H.S. Lee, X. Zuo, B. Lee, W. Fan, D.G. Vlachos, R.F. Lobo, M. Tsapatsis, P.J. Dauenhauer, Tunable oleo-furan surfactants by acylation of renewable furans, ACS Cent. Sci. 2 (11) (2016) 820–824, http://dx.doi.org/10.1021/acscentsci.6b00208.

[22] E.G. Derouane, D.J. Dillon, D. Bethell, S.B. Derouane-Abd Hamid, Zeolite catalysts as solid solvents in fine chemicals synthesis: 1. Catalyst deactivation in the Friedel–Crafts acetylation of anisole, J. Catal. 187 (1999) 209–218, http://dx.doi.org/10.1016/jcat.1999.2575.

[23] E.G. Derouane, G. Crehan, D.J. Dillon, D. Bethell, S.B. Derouane-Abd Hamid, Zeolite catalysts as solid solvents in fine chemicals synthesis: 2. Competitive adsorption of the reactants and products in the Friedel–Crafts acetylations of anisole and toluene, J. Catal. 194 (2000) 410–423, http://dx.doi.org/10.1016/jcat.2000.2933.

[24] P. Botella, A. Corma, J.M. López-Nieto, S. Valencia, R. Jacquot, Acylation of toluene with acetic anhydride over Beta zeolites: Influence of reaction conditions and physicochemical properties of the catalyst, J. Catal. 195 (2000) 161–168, http://dx.doi.org/10.1006/jcat.2000.2971.

[25] Y. Ji, J. Pan, P. Dauenhauer, R.J. Gorte, Probing direct carbon–carbon acylation of furans and long-chain acids over H-ZSM-5, Appl. Catal. A 577 (January) (2019) 107–112, http://dx.doi.org/10.1016/j.apcata.2019.03.012.

[26] M.G. Martin, J.I. Siepmann, Novel Configurational-Bias Monte Carlo Method for Branched Molecules. Transferable Potentials for Phase Equilibria. 2. United-atom description of branched alkanes, J. Phys. Chem. B 103 (21) (1999) 4508–4517, http://dx.doi.org/10.1021/jp984742e.

[27] A.Z. Panagiotopoulos, N. Quirke, M. Stapleton, D.J. Tildesley, Phase equilibria by simulation in the Gibbs ensemble alternative derivation, generalization and application to mixture and membrane equilibria, Mol. Phys. 63 (4) (1988) 527–545, http://dx.doi.org/10.1080/00268978800100361.

[28] A.Z. Panagiotopoulos, Direct determination of phase coexistence properties of fluids by Monte Carlo simulation in a new ensemble, Mol. Phys. 61 (4) (1987) 813–826, http://dx.doi.org/10.1080/00268978700101491.

[29] B. Smit, P. De Smedt, D. Frenkel, Computer simulations in the Gibbs ensemble, Mol. Phys. 68 (4) (1989) 931–950, http://dx.doi.org/10.1080/00268978900102641.

[30] J.I. Siepmann, M.G. Martin, B. Chen, C.D. Wick, J.M. Stubbs, J.J. Potoff, B.L. Eggimann, K.A. Maerzke, S.J. Keasler, P. Bai, E.O. Fetisov, M.S. Shah, Q.P. Chen, R.F. DeJaco, J.L. Chen, X. Bai, Y.-Z.-S Sun, Monte Carlo for Complex Chemical Systems–Minnesota, 2019.

[31] T.J.H. Vlugt, M.G. Martin, B. Smit, J.I. Siepmann, R. Krishna, Improving the efficiency of the configurational-bias Monte Carlo algorithm, Mol. Phys. 94 (1998) 727–733.

[32] J.I. Siepmann, D. Frenkel, Configurational bias Monte Carlo: A new sampling scheme for flexible chains, Mol. Phys. 75 (1) (1992) 59–70, http://dx.doi.org/10.1080/00268979200100061.

[33] J.J. De Pablo, M. Laso, J.I. Siepmann, U.W. Suter, Continuum-configurational-bias Monte Carlo simulations of long-chain alkanes, Mol. Phys. 80 (1993) 55–63, http://dx.doi.org/10.1080/00268979300102061.

[34] G.C.A.M. Mooij, D. Frenkel, B. Smit, Direct simulation of phase equilibria of chain molecules, J. Phys.: Condens. Matter 4 (16) (1992) L255–L259, http://dx.doi.org/10.1088/0953-8984/4/16/001.

[35] M. Laso, J. de Pablo, U. Suter, Simulation of phase equilibria for chain molecules, J. Chem. Phys. 97 (1992) 2817–2819, http://dx.doi.org/10.1063/1.463022.

[36] I. McDonald, NpT-ensemble Monte Carlo calculations for binary liquid mixtures, Mol. Phys. 23 (1) (1972) 41–58, http://dx.doi.org/10.1080/00268977200100031.

[37] R. DeJaco, MCFlow Software Package, 2019, URL https://github.com/dejac001/MCFlow.

[38] M.G. Martin, J.I. Siepmann, Transferable Potentials for Phase Equilibria. 1. United-atom description of n-alkanes, J. Phys. Chem. B 102 (14) (1998) 2569–2577, http://dx.doi.org/10.1021/jp972543+.

[39] G. Kamath, F. Cao, J.J. Potoff, An improved force field for the prediction of the vapor–liquid equilibria for carboxylic acids, J. Phys. Chem. B 108 (37) (2004) 14130–14136, http://dx.doi.org/10.1021/jp048581s.

[40] N. Rai, J.I. Siepmann, Transferable Potentials for Phase Equilibria. 9. Explicit hydrogen description of benzene and five-membered and six-membered hetero-cyclic aromatic compounds, J. Phys. Chem. B 111 (36) (2007) 10790–10799, http://dx.doi.org/10.1021/jp0735861.

[41] P. Bai, M. Tsapatsis, J.I. Siepmann, Trappe-zeo: Transferable Potentials for Phase Equilibria force field for all-silica zeolites, J. Phys. Chem. C 117 (46) (2013) 24375–24387, http://dx.doi.org/10.1021/jp4074224.

[42] J.L. Rafferty, L. Zhang, J.I. Siepmann, M.R. Schure, Retention mechanism in reversed-phase liquid chromatography: A molecular perspective, Anal. Chem. 79 (17) (2007) 6551–6558, http://dx.doi.org/10.1021/ac0705115.

[43] A. Farzaneh, R.F. DeJaco, L. Ohlin, A. Holmgren, J.I. Siepmann, M. Grahn, Comparative study of the effect of defects on selective adsorption of butanol from butanol/water binary vapor mixtures in silicalite-1 films, Langmuir 33 (34) (2017) 8420–8427, http://dx.doi.org/10.1021/acs.langmuir.7b02097.

[44] P. Bai, M. Tsapatsis, J.I. Siepmann, Multicomponent adsorption of alcohols onto silicalite-1 from aqueous solution: Isotherms, structural analysis, and assessment of ideal adsorbed solution theory, Langmuir 28 (44) (2012) 15566–15576, http://dx.doi.org/10.1021/la303247c.

[45] H. Van Koningsveld, H. Van Bekkum, J.C. Jansen, On the location and disorder of the tetrapropylammonium (TPA) ion in zeolite ZSM-5 with improved framework accuracy, Acta Crystallogr. B 43 (2) (1987) 127–132, http://dx.doi.org/10.1107/S0108768187098173.

[46] A. Ben-Naim, Statistical Thermodynamics for Chemists and Biochemists, first ed., Plenum Press, New York, 1992.

[47] M.G. Martin, J.I. Siepmann, Calculating Gibbs free energies of transfer from Gibbs ensemble Monte Carlo simulations, Theor. Chem. Acc. 99 (5) (1998) 347–350, http://dx.doi.org/10.1007/s002140050345.

[48] I.Y. Torshin, I.T. Weber, R.W. Harrison, Geometric criteria of hydrogen bonds in proteins and identification of 'bifurcated' hydrogen bonds, Protein Eng. 15 (5) (2002) 359–363, http://dx.doi.org/10.1093/protein/15.5.359.

[49] J.M. Stubbs, J.I. Siepmann, Elucidating the vibrational spectra of hydrogen-bonded aggregates in solution: Electronic structure calculations with implicit solvent and first-principles molecular dynamics simulations with explicit solvent for 1-hexanol in n-hexane, J. Am. Chem. Soc. 127 (2005) 4722–4729, http://dx.doi.org/10.1021/ja044380q.

[50] E.W. Lemmon, M.O. McLinden, D.G. Friend, Thermophysical properties of fluid systems, in: P. Linstrom, W. Mallard (Eds.), NIST Chemistry WebBook, NIST Standard Reference Database Number 69, National Institute of Standards and Technology, Gaithersburg, MD, 2020, http://dx.doi.org/10.18434/T4D303.

[51] D.L. Morgan, R. Kobayashi, Direct vapor pressure measurements of ten n-alkanes in the C10–C28 range, Fluid Phase Equilib. 97 (C) (1994) 211–242, http://dx.doi.org/10.1016/0378-3812(94)85017-8.

[52] A.Z. Panagiotopoulos, Adsorption and capillary condensation of fluids in cylindrical pores by Monte Carlo simulation in the Gibbs ensemble, Mol. Phys. 62 (3) (1987) 701–719, http://dx.doi.org/10.1080/00268978700102501.

[53] M. Thommes, G.H. Findenegg, Pore condensation and critical-point shift of a fluid in controlled-pore glass, Langmuir 10 (11) (1994) 4270–4277, http://dx.doi.org/10.1021/la00023a058.

[54] M. Thommes, K. Kaneko, A.V. Neimark, J.P. Olivier, F. Rodriguez-Reinoso, J. Rouquerol, K.S. Sing, Physisorption of gases, with special reference to the evaluation of surface area and pore size distribution (IUPAC Technical Report), Pure Appl. Chem. 87 (9–10) (2015) 1051–1069, http://dx.doi.org/10.1515/pac-2014-1117.

[55] B.L. Severson, R.Q. Snurr, Monte Carlo simulation of n-alkane adsorption isotherms in carbon slit pores, J. Chem. Phys. 126 (13) http://dx.doi.org/10.1063/1.2713097.

[56] T.K. Xia, O.Y. Jian, M.W. Ribarsky, U. Landman, Interfacial alkane films, Phys. Rev. Lett. 69 (1992) 1967–1970, http://dx.doi.org/10.1103/PhysRevLett.69.1967.

[57] S. Balasubramanian, M.L. Klein, J.I. Siepmann, Monte Carlo investigations of hexadecane films on a metal substrate, J. Chem. Phys. 103 (1995) 3184–3195, http://dx.doi.org/10.1063/1.470251.

Paul Dauenhauer received a bachelor of science in chemical engineering and chemistry from the University of Wisconsin, Madison, in 2004 and a Ph.D. in chemical engineering from the University of Minnesota in 2008. From 2008 to 2009, Paul worked as a senior research engineer for the Dow Chemical Company within Core R&D in Midland, MI and Freeport, TX. In 2009, he joined the University of Massachusetts, Amherst, Department of Chemical Engineering as an assistant professor. He is currently the Lanny Schmidt Honorary Professor at the University of Minnesota in the Department of Chemical Engineering and Materials Science.
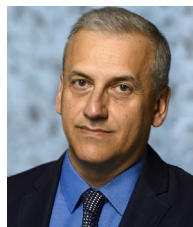
Michael Tsapatsis is a Bloomberg Distinguished Professor of Chemical and Biomolecular Engineering at Johns Hopkins University (JHU) with a joint appointment in the Applied Physics Laboratory. His research group's accomplishments include development of hierarchical mesoporous zeolite catalysts, oriented molecular sieve films, molecular sieve/polymer nanocomposites for membrane applications, crystal structure determination of adsorbents that are now used in a commercial process, and synthesis of precisely sized oxide nanoparticles that have been commercialized. He is a fellow of the American Association for the Advancement of Science (2011) and member of the National Academy of Engineering (2015).

Tyler Josephson is an Assistant Professor at the University of Maryland, Baltimore County in Chemical, Biochemical, and Environmental Engineering. He received a B.S. in Chemical Engineering from the University of Minnesota (2011) and a Ph.D. in Chemical Engineering from the University of Delaware (2017), working with D.G. Vlachos and S. Caratzoulas. He was a postdoctoral researcher in the Department of Chemistry at the University of Minnesota (2017–2020), working with J.I. Siepmann. His research group, the ATOMS lab (AI & Theory-Oriented Molecular Science), uses molecular simulation and machine learning to gain molecular-scale insights to enable solutions for cleaner air and water.

Ilja Siepmann is a Professor of Chemistry, Distinguished McKnight University Professor, Distinguished Teaching Professor, and member of the graduate faculties in chemical physics, chemical engineering, and materials science at the University of Minnesota. He received his Ph.D. in Chemistry from the University of Cambridge. Before joining the University of Minnesota in 1994, Dr. Siepmann carried out postdoctoral research at the IBM Zurich Research Laboratory, the Royal/Shell Laboratory in Amsterdam, and the University of Pennsylvania's Laboratory for the Research on the Structure of Matter. His scientific interests are focused on particle-based simulations of complex chemical systems.